

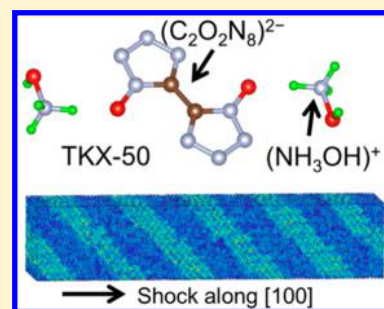
Anisotropic Impact Sensitivity and Shock Induced Plasticity of TKX-50 (Dihydroxylammonium 5,5'-bis(tetrazole)-1,1'-diolate) Single Crystals: From Large-Scale Molecular Dynamics Simulations

Qi An,[‡] Tao Cheng,[‡] William A Goddard, III,^{*} and Sergey V. Zybin

Materials and Process Simulation Center, California Institute of Technology, Pasadena, California 91125, United States

S Supporting Information

ABSTRACT: Dihydroxylammonium 5,5'-bis(tetrazole)-1,1'-diolate (TKX-50) is a newly synthesized energetic material with high energy storage, low impact sensitivity, and low toxicity. These features make it a viable candidate to replace such commonly used energetic materials as RDX and CL-20 in the next generation of explosives. Sensitivity determines the engineering application of energetic materials (EMs) and has been widely studied for various EMs. To understand the origin of the anisotropic sensitivity and properties of this new synthesized EM, we report a flexible classical force field for TKX-50 developed to reproduce the molecular properties (geometry, vibrational frequencies and torsion barriers) and the crystal properties (cell parameters and lattice energy). We then used this force field in molecular dynamics (MD) simulations to predict such thermodynamic and mechanical properties as isothermal compressibility, thermal expansion, elastic moduli, and heat capacity. Furthermore, we carried out large scale (~a half million atoms) MD simulations to investigate the mechanical response to shocks in the [100], [010] and [001] directions. The predicted Hugoniot elastic limits (HELs) are 6.1 GPa for [100], 14.2 GPa for [010] and 9.1 GPa for [001] shocks. Thus, single crystal TKX-50 shows anisotropic impact sensitivity with [010] as the most sensitive direction and [100] as least sensitive. The plastic deformations in shock compression along the [100] direction primary arise from the (001)/[210] and (010)/[001] slip systems of. For the [010] shock, the primary slip systems are (100)/[021] and (001)/[210]. However, no obvious slip system was observed for [001] shock.



1. INTRODUCTION

Dihydroxylammonium 5,5'-bis(tetrazole)-1,1'-diolate (TKX-50) is a newly synthesized explosive^{1–3} that is easily prepared and exceedingly powerful, while being insensitive both for thermal and shock impact, with low toxicity. These features make it a promising candidate to replace such widely used explosives as hexahydro-1,3,5-trinitro-1,3,5-triazine (RDX),⁴ octahydro-1,3,5,7-tetranitro-1,3,5,7-tetrazocine (HMX),⁵ and 2,4,6,8,10,12-hexanitro-2,4,6,8,10,12-hexaza-isowurtzitane (CL-20).⁶ TKX-50 outperforms these widely used explosives as follows.

- TKX-50 has a calculated detonation velocity of 9698 m/s that is 700 m/s higher than RDX and 250 m/s higher than CL-20.¹
- TKX-50 possesses substantially lower impact sensitivity (20 J) compared with RDX (7.5 J) and CL-20 (4 J),¹ making it much safer for resisting unintentional detonation due to shocks. The friction sensitivity for TKX-50 is 120 N, which is comparable or lower than other popular EMs: RDX (120 N), β -HMX (112 N), and CL-20 (48 N).¹ TKX-50 starts to decompose at 221 °C, which is higher than RDX (210 °C) and CL-20 (215 °C).¹
- The synthetic routes for TKX-50 are simple and scalable, which is essential for commercial manufacture. In

contrast, high performance explosives such as dinitroazofuroxan (DDF) and octanitrocubane (ONC) with detonation velocities of ~10 000 m/s require extremely a complex synthetic processes (ten or more steps) making them impractical for industrial production.

- Toxicity is a growing concern of energetic materials based on new understanding of the fate of explosives in the environment. The ubiquitous nitramine content of the RDX and CL-20 has been shown to be toxic to vital organisms, such as earthworms, at the base of the food chain. In addition, RDX is a probable human carcinogen. TKX-50 is much less toxic to the airways, making it less of a health risk than RDX if inhaled.¹

Sensitivity is a very important parameter for energetic materials (EMs). Since the improved performance TKX-50 over current widely used explosives makes it a promising future explosive, it is important to examine its sensitivity and mechanical response under shock compression. However, no shock experiment data is available for TKX-50. Recently we used quantum mechanics (QM) MD simulations to examine the reaction mechanisms underlying the initial steps in the

Received: October 31, 2014

Revised: December 23, 2014

Published: December 29, 2014

thermal decomposition of TKX-50, showing that proton transfer from hydroxylammonium (NH_3OH^+) cation to the diolate ($\text{C}_2\text{O}_2\text{N}_8$)²⁻ dianion decreases the initial reaction barrier of ring breaking for N_2 release.⁷

It is generally accepted that detonation of explosives is initiated at hot-spots^{8,9} with defects such as voids and interfaces playing essential roles.^{10–12} For a single crystal, the hotspot can initiate through formation of dislocation pile-up that is released by plasticity deformation, heating at the crack tip, and chemical decomposition.¹³ Thus, it is essential to examine the plastic deformation of TKX-50 in shock compression along various shock directions to understand the origin of anisotropic detonation sensitivity.

To understand the material properties and provide insight into the atomistic mechanisms, many classical force fields (FFs) have been developed for energetic materials, such as TATB,^{14,15} RDX,^{16,17} HMX,¹⁸ AN,¹⁹ and TNT.²⁰ These FFs have been widely used in molecular dynamics simulations to examine the structural, thermal, and mechanical properties, providing much useful information in addition to the experiments.^{21–25} Especially, MD simulations of shock compression provide atomistic deformation mechanism of explosives under high strain rate compression.^{21,22}

In this paper, we report large scale MD using FFs determined from quantum mechanics (QM) to examine the atomistic mechanism underlying the favorable mechanical properties of TKX-50. Reactive FFs have previously been employed to examine chemical reactivity, anisotropic sensitivity, and hotspot formation in single crystals and polymer bonded explosives.^{10,12,26–30} But here we developed a nonreactive FF to examine plastic deformation of energetic materials, without chemical reactions. This new flexible classical FF for TKX-50 reproduces the molecular structures (bond length, angle and torsion angle), vibrational frequencies and torsion barriers for finite molecules as well as the crystal structure and cohesive energy.

Using this newFF, we predicted thermodynamic properties including heat capacity, isothermal compressibility, and mechanical properties including bulk modulus and shear modulus. Large scale MD simulations were performed to examine the mechanical response and the anisotropic plasticity and sensitivity under shock compression along three crystallographic orientations: [100], [010], and [001].

2. DEVELOPMENT OF A FLEXIBLE CLASSICAL FORCE FIELD

2.1. First-Principles Calculations. To obtain the training set database for the force field development, we carried out the DFT calculations on the TKX-50 molecule and crystal. Structure optimization and frequency calculation of finite molecules were carried out at the level of B3LYP/6-311G** using the Jaguar 7.7 software.^{31–33}

The periodic crystal calculations were performed using Perdew–Burke–Ernzerhof (PBE) exchange–correlation functional with the projector augmented wave method to account for core–valence interactions as implemented in VASP and modified to include the London dispersion interactions (van der Waals attraction, PBE-ulg method).^{34–38} The kinetic energy cutoff for plane wave expansions was set to 500 eV, and the reciprocal space was sampled by Γ -centered Monkhorst–Pack scheme with a fine resolution of $2\pi \times 1/60 \text{ \AA}^{-1}$. The calculated cell parameters from PBE-ulg are $a = 5.116 \text{ \AA}$, $b = 12.260 \text{ \AA}$, $c = 6.775 \text{ \AA}$, and $\beta = 95.9^\circ$, consistent with

experimental values at 300 K of $a = 5.441 \text{ \AA}$, $b = 11.751 \text{ \AA}$, $c = 6.561 \text{ \AA}$, and $\beta = 95.1^\circ$.¹ To extract the charges in the crystal phase, we used the self-consistent charge density functional tight binding (SCC-DFTB) method³⁹ with the DFTB3–3OB parameter set.⁴⁰

2.2. Force Field Function Form and Parametrization. We used the AMBER form²⁶ for the potential energy function

$$E = \sum_{\text{bonds}} K_r(r - r_0)^2 + \sum_{\text{angles}} K_\theta(\theta - \theta_0)^2 + \sum_{\text{torsions}} \frac{V_n}{2}[1 + \cos(n\varphi - \gamma)] + \sum_{\text{improper}} \frac{K_\chi}{2}[1 + \cos(n\chi - \chi_0)] + \sum_{i < j}^{\text{atoms}} 4\epsilon_{ij} \left[\left(\frac{\sigma_{ij}}{r_{ij}} \right)^{12} - \left(\frac{\sigma_{ij}}{r_{ij}} \right)^6 \right] + \sum_{i < j}^{\text{atoms}} \frac{q_i q_j e^2}{r_{ij}} \quad (1)$$

where the six terms include the energies of bond stretching, angle bending, torsional motion, improper torsion, Coulomb interactions, and van der Waals interactions. Detailed explanations of the parameters in eq 1 are found elsewhere.⁴¹

The interactions between different atomic types are computed using standard Lorentz–Berthelot combination rules:

$$\sigma_{ij} = (\sigma_{ii} + \sigma_{jj})/2 \quad (2)$$

$$\epsilon_{ij} = \sqrt{\epsilon_{ii}\epsilon_{jj}} \quad (3)$$

The electrostatic interactions and van der Waals interactions for next–next nearest neighbors (1–4 interactions) are scaled by 0.5.

We used the Direct Force Field (DFF)⁴² package to determine the FF parameters. The valence parameters were determined by fitting to QM data including energy, force, frequency, and torsion barriers. The vdW parameters were fitted to experimental cell parameters, densities, and lattice energy. In the fitting procedure, we first determined the atomic charges, then the valence parameters, and finally the vdW parameters. Using the new vdW parameters, we performed new iterations (with fixed charges) to ensure that the valence parameters remain accurate. The Levenberg–Marquardt minimization method was used to determine the valence terms. The Hessian matrix was used to derive the force constants for the valence terms. We did not include the eigenvectors in the training process.^{43,44} The FF parameters are given in Table 1 and Tables S1–S5 of the Supporting Information.

The crystal structure of TKX-50 (P_{21}/c space group) is shown in Figure 1. The unit cell consists of two bistetrazole anions (formal charge -2) and four hydroxylammonium (NH_3OH^+) cations (formal charge of $+1$). The molecular structures of olate and hydroxylammonium are shown in Figure 2.

Various approaches have been proposed to determine the atomic charges:⁴⁵ Mulliken populations and Löwdin populations,^{46,45} atoms in molecules theory,⁴⁷ empirical approaches to reproduce crystallographic⁴⁸ or liquid data,⁴⁹ Bader charges for crystals, the electrostatic potential (ESP) derived charges based on semiempirical⁵⁰ or *ab initio* methods,^{51–56} and AM1-BCC charges.^{57,58} In this paper, we employed the self-consistent

Table 1. Force Field Parameters^a

	atom	atom type	charge	ϵ_i (kcal/mol)	δ_i (Å)
olate	O1	o_1	-0.5832	0.210	2.346
	C1	c_35	0.0760	0.076	3.091
	N1	n_3	0.4174	0.145	3.913
	N2	n_25	-0.2030	0.170	2.789
	N3	n_25	-0.2030	0.170	2.789
	N4	n_25c	-0.2432	0.170	2.304
Ammonium	N5	n_4+	0.1288	0.145	3.565
	O2	o_2	-0.3592	0.170	2.591
	H(N)	h_1n	0.1936	0.030	2.115
	H(O)	h_1o	0.3056	0.001	1.909

^aSee eq 1 for definitions and Figure 2 for atom labels. Lorentz–Berthelot combination rules in eq 2 and 3 are used for different atom types. All 1–2 and 1–3 intramolecular electrostatic interactions and van der Waals interactions are excluded. A scale factor of 0.5 is applied to 1–4 intramolecular electrostatic interactions and van der Waals interactions. The QM charges were derived using the DFTB-SCC method. They are further scaled by 0.8 to be used in the FF. The total charges for olate and hydroxylammonium are -1.312, and +0.656 in the FF, which can be compared with the QM values of -1.640 and +0.820.

charge (SCC) scheme to extract the atomic charge with a $(4 \times 2 \times 3)$ supercell, in which the Mulliken charges are redistributed self-consistently. The QM charges were further scaled by a factor of 0.8 to reproduce the lattice energy. Table 1 lists the atomic charges used in the force field (from SCC and scaled by 0.8).

Each tetrazole ring has six π -electrons (four from the CN and NN double bonds and two from the $p\pi$ orbital of the N bonded to OH) providing aromatic stability. The O^- anions contribute additional resonance structures from the $p\pi$ lone pair. As a result, all bonds in olate anions show partial double bond character (shown in Table 2). To fit the valence parameters of the FF, we could use the finite olate anion. However, the bond lengths in olate deviate substantially from the corresponding bonds in the crystal as shown in Table 2. Thus, the N–O bond of olate (N1–O1) is too short (1.283 Å compared with 1.328 Å in crystal) indicating that N–O is too conjugated. This makes all other bonds longer than those in the crystal. Also, the trend of N3–N4 and N1–N2 is opposite: in the crystal, N1–N2 is longer, but for the finite molecule, N3–N4 is longer. This discrepancy arises because the charges in the crystal are partially

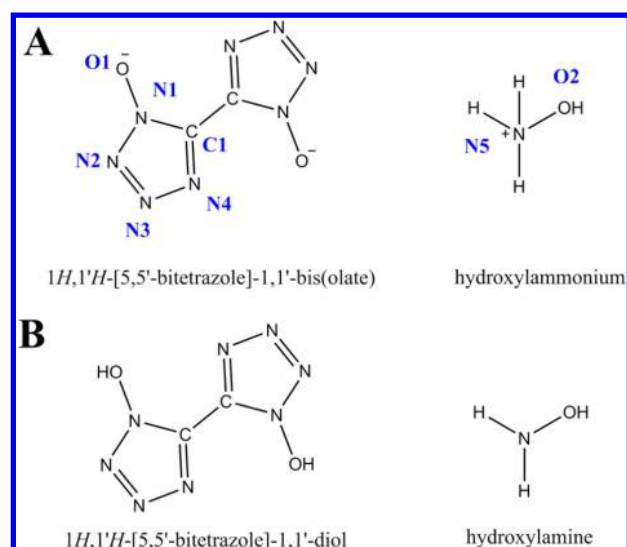


Figure 2. (A) Molecular structures of the anion (−2 formal charges), olate (1H,1'H-[5,5'-bis(tetrazole)]-1,1'-bis(olate)) and the cation (+1 formal charge), hydroxylammonium. (B) Molecular structures of the neutral molecular structures: diols (1H,1'H-[5,5'-bis(tetrazole)]-1,1'-diol) and hydroxylamine. N1 to N5 and O1 to O2 are used to distinguish the N and O positions in the tetrazole ring.

Table 2. Comparison of the Bond Lengths (in Å) for Various Bond Types (Figure 2) of Olate, Diol, and Crystal^a

bond type	bond length (Å)			
	olate	diol	crystal (FF)	crystal (exptl at 100 K)
C1–C1	1.454	1.427	1.449	1.445(3)
C1–N1	1.378	1.342	1.359	1.345(18)
C1–N4	1.347	1.325	1.333	1.336(17)
N1–O1	1.283	1.359	1.335	1.328(16)
N1–N2	1.358	1.332	1.354	1.343(16)
N2–N3	1.322	1.302	1.311	1.313(17)
N3–N4	1.335	1.352	1.348	1.352(17)

^aThe molecular structures of olate and diol are obtained from QM (B3LYP/6-311G**). For the crystal, both the experimental value (at 100 K) and the force field value are shown here. The intramolecular parameters are trained to the Diol QM structures, and then further refined to reproduce the experiment bond lengths. The labels of atoms are the same as Figure 2 and Table 1.

delocalized back onto the cations. On the other hand, adding one H to each O^- to form the diol, leads to a QM geometry in

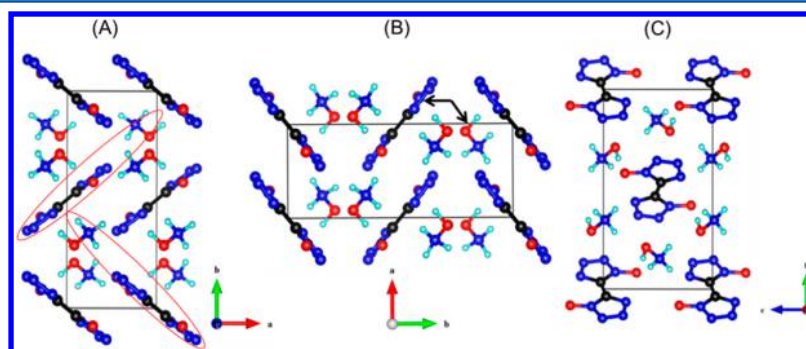


Figure 1. Crystal structure of TKX-50 at room temperature taken from experiment.¹ The space group is P_{21}/c . Atoms colored as N in blue, O in red, H in cyan, and C in black. The bistetrazole ring along b direction is shifted by $1/2$ unit cell to its neighbor bis(tetrazole). The red circle and the arrows refer to the two molecules in the same layer. Parts A and B are the view from the “ c ” direction, and part C is the view from the “ a ” direction.

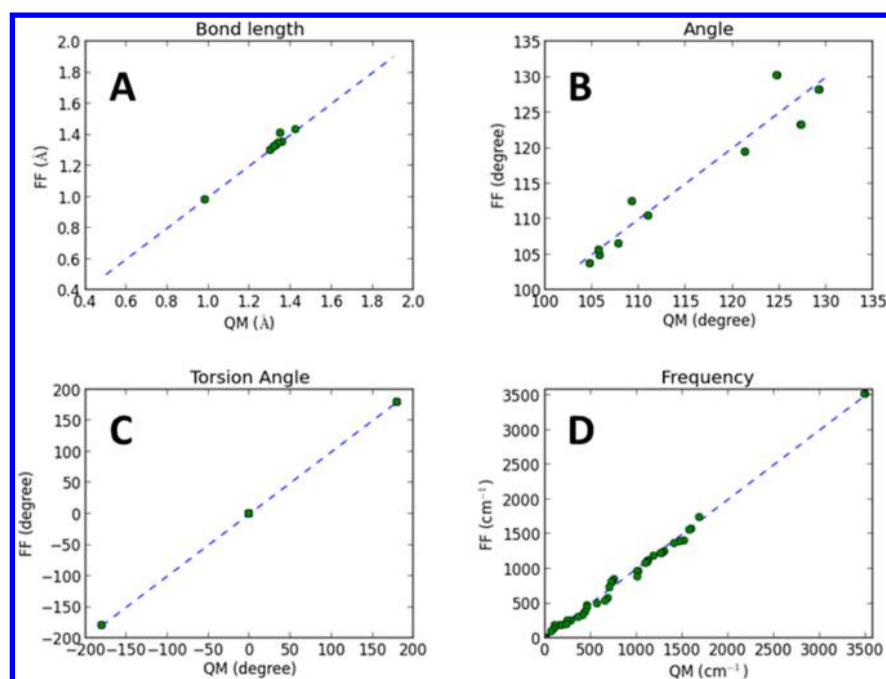


Figure 3. Comparison geometric parameters of the optimized diol molecule (shown in Figure 2) from FF and QM: (A) bond lengths (in Å), (B) angles (in degrees), (C) torsion angles (in degrees), and (D) frequencies (in cm^{-1}). The blue slashed line is the diagonal for viewing convenience.

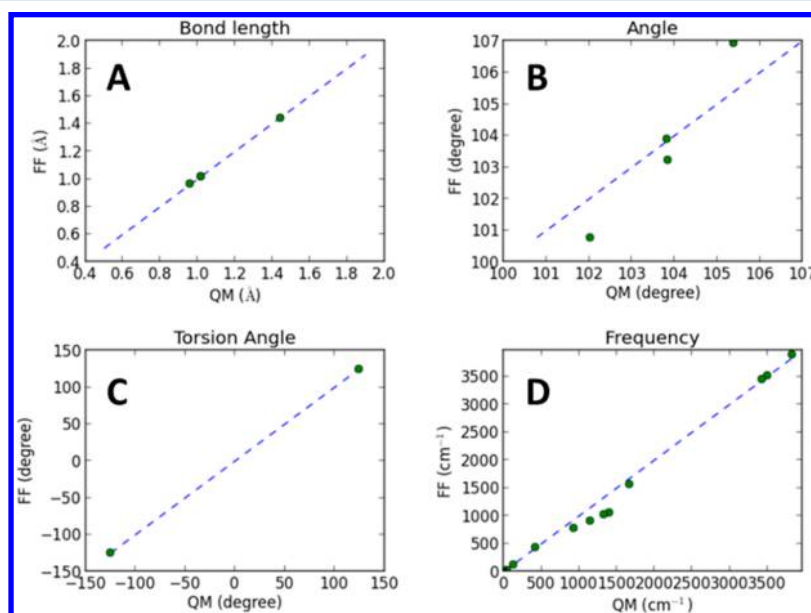


Figure 4. Comparison geometric parameters of the optimized hydroxylamine molecule (shown in Figure 2) from FF and QM: (A) bond lengths (in Å), (B) angles (in degrees), (C) torsion angles (in degree), and (D) frequencies (in cm^{-1}). The blue slashed line is the diagonal for viewing convenience.

good agreement with crystal, as shown in Figure 2 (B) and compared in Table 2. Thus, we used the diol structure to fit the valence parameters, including bond length, angles, torsion angles, and frequencies.

The valence parameters were fitted to the energy, gradient, and Hessian from the QM and are listed in Table S1 of the Supporting Information. The bond lengths, angles, torsion angles, and frequencies from the FF are compared with QM in Figure 3, showing good agreement. The average deviation for bond lengths, angles and torsion angles are 0.007 Å , -0.28° , and 0.0008° , respectively. The maximum deviation for lengths, angles and torsion angles are 0.06 Å , 5.48° and 0.065° ,

respectively. The mass weighted Hessian was diagonalized to obtain frequencies.

Although the above fitting is good, the geometry still deviates from that in crystal, which would lead to errors in the crystal structure and density. To reproduce the crystal structure and density, we further adjusted the bond lengths based on molecules in crystal structure, but leaving the force constants unchanged. This adjustment on the bond distances is within 2%, which has no effect on the frequencies. In this way, the FF is improved to reproduce geometries without sacrificing accuracy in frequencies. The optimized bond lengths using

the improved force field are shown in Table 2, showing good agreement with experiment.

Figure 4 shows the results of fitting the FF for hydroxylamine, again consistent with QM. The mean deviations for bond lengths, angles and torsion angles are -0.0016 Å, -0.067° , and 0.052° , respectively. The maximum deviation for lengths, angles and torsion angles are 0.0085 Å, 1.54° , and -0.79° , respectively.

To fit the torsion barrier of N–C–C–N and H–O–N–H, we scanned the N–C–C–N (in diol) from 0 to 360° and the H–O–N–H (in hydroxylamine) from -120° to $+240^\circ$ with a step of 30° . The potential energy surfaces of N–C–C–N from QM and FF are shown in Figure 5. The energy barrier from

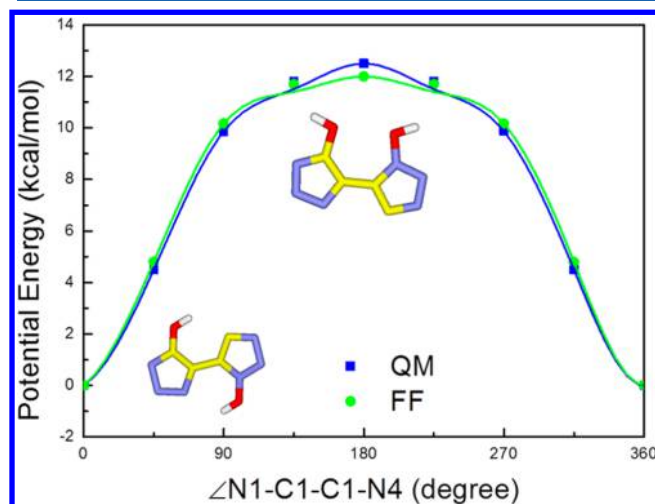


Figure 5. Comparison of the N1–C1–C1–N4 torsion barrier (in kcal/mol) between FF and QM. Here, the blue square is from QM and the green dots and line are from the FF. The configurations of 0° and 180° are shown in the figure. The yellow part shows the N–C–C–N torsion angle.

QM is 12.43 kcal/mol, with the maximum located at 180° . The potential energy surface of H–O–N–H along the torsion angle is shown in Figure 6. Two potential energy barriers were

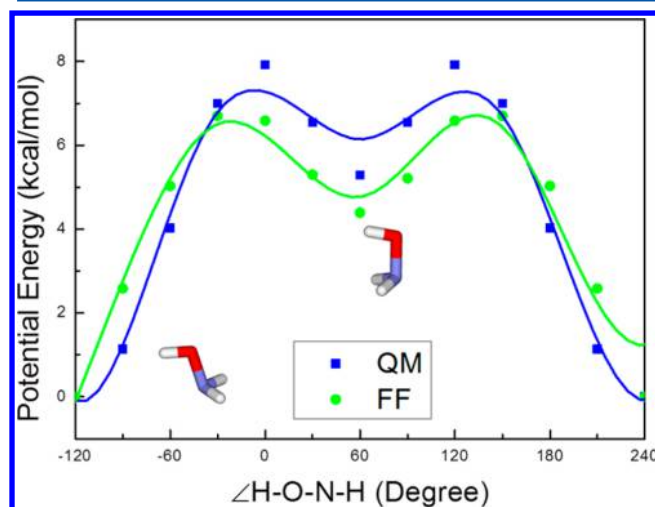


Figure 6. Comparison of the H–O–N–H torsion barrier (in kcal/mol) between FF and QM. Here, the blue line is from QM and the green dots and line are from FF. The configurations of -120° and $+60^\circ$ are shown in the subfigures.

observed at 0° and 120° . At 60° , the potential energy is about 2.5 kcal/mol lower (~ 5.5 kcal/mol). The comparison between FF and QM shows that the FF reproduces these two torsion barriers with errors within 1 kcal/mol.

The vdW parameters were fitted to reproduce the experimental cell parameters (Table 3) at 298 K and the cohesive energy. Since there are more vdW parameters (nine atom types with 9 vdW radius plus 9 vdW well depths) than crystal parameters, we started with Amber parameters and scaled all the parameters simultaneously (keep the relative ratios fixed) to obtain the correct total pressure of 1.0 bar. Then we adjusted the H and O parameters to obtain the correct cell parameters (a , b , c , α , β , and γ). The final force field reproduces the cell parameters and density at 298 K. The comparison between FF and experiments is shown in Table 3, where the FF reproduces the cell length in the c direction but underestimates it by 3.5% in the a direction, and overestimates it by 3.1% in the b direction. These errors cancel, leading to the density of 1.875 g/cm 3 that matches the experimental value of 1.877 g/cm 3 .¹

3. PREDICTED THERMODYNAMIC AND MECHANICAL PROPERTIES

We extracted the thermodynamic properties and mechanical properties with the new FF using MD simulations. The MD simulations were carried out using LAMMPS package,⁵⁹ using the particle particle particle mesh (PPPM) method⁶⁰ for the electrostatic interaction to an accuracy of 10^{-4} . The Coulomb and vdW cut-offs were both set to 9.5 Å. Cubic splines were used to cutoff the vdW interaction, with $R_{\text{inner}} = 8.5$ Å and $R_{\text{outer}} = 9.5$ Å.

The MD time step is 0.5 fs. We applied various ensembles in the MD simulations including NVT (constant volume, constant temperature, and constant number of particles), NPT (constant volume, constant pressure, and constant number of particles) and NVE (microcanonical). The thermostat and barostat used the Nose-Hoover style⁶¹ with damping constants for temperature of 100 fs and for pressure of 1000 fs.

We started with a $(4 \times 2 \times 3)$ supercell replicated from the experimental unit cell. The initial structure was first minimized using the conjugate gradient (CG) method, and then followed by a NVT simulation at 100 K for 20 ps. We then carried out cook-off simulations to heat the system uniformly from 100 to 400 K within 20 ps. Then we equilibrated the system at particular temperatures using NPT simulations for 500 ps to predict the densities and the cell parameters, using the averages over the last 200 ps. To extract the fluctuation properties, such as isothermal compressibility and thermal expansion coefficient, we performed 5 ns MD simulations. To derive the heat capacity, we used the two-phase thermodynamic (2PT) method^{62,63} from a 100 ps NVT simulation trajectory (saved every 2 fs) to calculate the vibrational density of states while eliminating diffusional effects.

3.1. Isothermal Compressibility. Under isothermal conditions, the relative volume change in response to pressure is the compressibility (κ_T), which is defined as

$$\kappa_T = -\frac{1}{V} \left(\frac{\partial V}{\partial p} \right)_T \quad (4)$$

This quality can be obtained using MD simulations by the volume fluctuation formula:⁶⁴

Table 3. Comparison of the Properties Calculated from the FF and QM with Experiment^a

properties	FF	QM	exptl
<i>a</i> (Å)	5.25(2)		5.4408(6) ^b
<i>b</i> (Å)	12.11(4)		11.7514(13) ^b
<i>c</i> (Å)	6.60(1)		6.5612(9) ^b
α (deg)	90		90 ^b
β (deg)	93.5		95.1 ^b
γ (deg)	90		90 ^b
volume (<i>V</i> , Å ³)	418(2)		417.86(9) ^b
density (ρ , g·cm ⁻³)	1.875(8)		1.877 ^b
lattice energy (kJ·mol ⁻¹)	-756(20)	-833.55 ^c	-1506 ^d
coefficient of thermal expansion (α_p , 10 ⁻⁶ K ⁻¹)	64.8		
isothermal compressibility (κ_T , J/m ⁻³)	3.863×10^{-11}		
heat capacity (<i>C_v</i> , J mol ⁻¹ K ⁻¹)	292(38)		
heat capacity (<i>C_p</i> , J mol ⁻¹ K ⁻¹)	295(43)		
bulk modulus (<i>K</i> , GPa)	32.719	31.578 ^c	
shear modulus (<i>G</i> , GPa)	12.385	9.067 ^c	

^aThe properties includes cell parameters (*a*, *b*, *c*, α , β , and γ), volume of unit cell, density, lattice energy, coefficient of thermal expansion (α_p), isothermal compressibility (κ_T), heat capacities (*C_v* and *C_p*), bulk modulus (*K*), and shear modulus (*G*). All data are calculated at room temperature except bulk modulus and shear modulus. ^bThe experimental data were taken from ref 1. ^cQM data were derived from at the level of PBE with low gradient corrections. ^dThe experimental data were taken from ref 72.

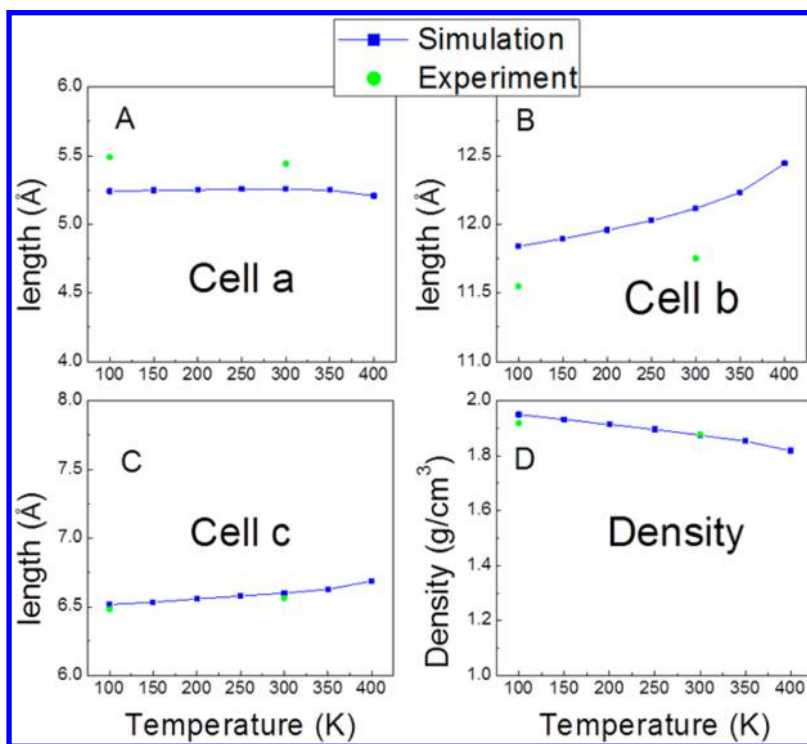


Figure 7. Comparison of the temperature dependent cell parameters of *a*, *b*, and *c* (from A to C) and density (D). The blue squares and line represent for FF values, and the green circles represent experimental values.

$$\kappa_T = \frac{\langle V^2 \rangle - \langle V \rangle^2}{k_B \langle T \rangle \langle V \rangle} \quad (5)$$

The predicted compressibility for TKX-50 at room temperature is 3.863×10^{-11} m³/J. The compressibility could also be obtained from the bulk modulus. On the basis of the QM derived bulk modulus in the following section, the compressibility for TKX-50 at 0 K is 3.167×10^{-11} m³/J. Our prediction of κ_T from fluctuation MD method agrees well with the value derived from the QM method.

3.2. Coefficient of Thermal Expansion. The coefficient of thermal expansion α_p is defined as

$$\alpha_p = \frac{1}{V} \left(\frac{\partial V}{\partial T} \right)_p \quad (6)$$

which can be extracted from MD simulations by the enthalpy–volume fluctuation formula:⁶⁴

$$\alpha_p = \frac{\langle VH \rangle - \langle V \rangle \langle H \rangle}{k_B \langle T \rangle^2 \langle V \rangle} \quad (7)$$

Figure 7 shows the temperature dependent density and cell parameters of *a*, *b*, and *c*. These curves reflect the balance of Coulomb and van der Waals interactions, which can be used to validate the charges. To compare with two available

experimental points (100 and 298 K), we performed four simulations at temperatures ranging from 100 to 400 K with a step of 100 K. Figure 7D shows the comparison of temperature dependent densities between force field and experiments. The calculated thermal expansion coefficient of $64.8 \times 10^{-6} \text{ K}^{-1}$ agrees well with experiments (deviation within 1%). In contrast, the thermal expansion coefficient for RDX⁶⁵ is $20.7 \times 10^{-5} \text{ K}^{-1}$ which is 3.2 times larger than TKX-50. This is because the ionic character of TKX-50 leads to much less expansion than the molecular crystal RDX. Figure 7A–C compares the temperature dependent cell parameters for FF and experiments. As the temperature increases, the cell length in the “*a*” direction nearly keeps constant. Only a small increase was observed in the “*c*” direction. Thus, the new FF captures this anisotropic expansion behavior of TKX-50.

3.3. Heat Capacities. We calculated the heat capacities with constant volume (C_v) from the vibrational density of states (DoS) from the 2PT analysis of the MD trajectory:^{62,63}

$$C_V = k_B \int_{-\infty}^{\infty} [\text{DoS}_{\text{gas}}(\nu) W_{\text{gas}}^{C_V}(\nu) + \text{DoS}_{\text{solid}}(\nu) W_{\text{solid}}^{C_V}(\nu)] d\nu \quad (8)$$

where DoS_{gas} and $\text{DoS}_{\text{solid}}$ represent the density of states in the gas phase and solid phase, and W_{gas} and W_{solid} are weighting factors for gas phase and solid phase. The 2PT analysis for C_v avoids the problem predicting heat capacities from classical simulations, because the quantum effects for each mode are included.

Experimentally, the heat capacity with constant pressure (C_p) is easier to measure than C_v . Thus, we correct the calculated value with the corrections in (9):

$$\begin{aligned} C_p &= \left(\frac{\partial H}{\partial T} \right)_p = C_v + \Delta C_{v,p} = C_v + T \left(\frac{\partial P}{\partial T} \right)_{N,V} \left(\frac{\partial V}{\partial T} \right)_{N,p} \\ &= C_v + VT \frac{\alpha_p^2}{\kappa_T} \end{aligned} \quad (9)$$

using α_p (coefficient of thermal expansion) and κ_T (isothermal compressibility).

The ratio of C_p/C_v is required in numerical models to construct the shock models, but no experimental data available had been available for TKX-50. Our predicted results are $C_p = 295 \text{ J mol}^{-1} \text{ K}^{-1}$ and $C_v = 292 \text{ J mol}^{-1} \text{ K}^{-1}$ at room temperature as shown in Table 3. In contrast, the experimental values of C_p at 320 K are $320 \text{ J mol}^{-1} \text{ K}^{-1}$ for HMX⁶⁶ and $\sim 242 \text{ J mol}^{-1} \text{ K}^{-1}$ for RDX.⁶⁷

3.4. Bulk Modulus and Shear Modulus. The bulk modulus (K) and shear modulus (G) contain information can be related to the hardness of a material for various types of deformation. Typically a third or fourth order Birch–Murnaghan equation of state is utilized. Alternatively, the bulk and shear modulus can be derived from the elastic constant tensor using Voight and Hill methods.⁶⁸

Figure 8 compares the equation of state (pressure vs volume) for the new force field and QM. The QM data were calculated from PBE-ulg calculations. The optimized cell volume was increased isotropically to 120% and decreased to 80%. The pressures derived from the force field agree with QM data well in the expansion region. In the compression region, force field overestimates the pressure, which comes from the LJ 12-6 functional form used for the vdW interactions, which is too repulsive at short-range.

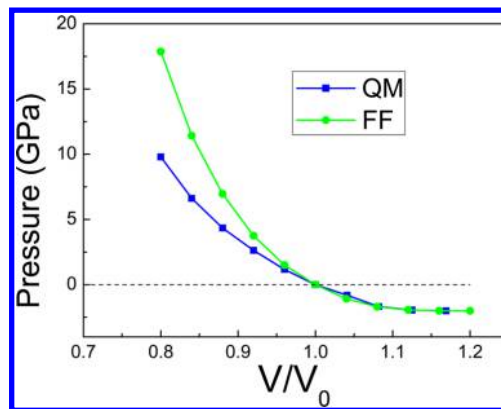


Figure 8. Comparison of the equation of state (pressure–volume) of TKX-50 crystal between FF and QM. Here, the blue line and squares stands for QM values, and the green dots and line stand for FF results. The slashed line labels the zero pressure for viewing convenience.

The bulk modulus of 32.719 GPa derived from the FF agrees well with the QM value of 31.578 GPa. The shear modulus derived from the FF of 12.385 GPa is 35% higher than the QM value of 9.067 GPa. These results are also listed in Table 3.

4. SHOCK COMPRESSION SIMULATIONS

4.1. Constant-Stress Hugoniot Simulations. For one-dimensional steady flow, the conservation of mass, momentum, and the energy across a planar shock front connecting the initial (unshocked) and final (shocked) states leads to the Rankine–Hugoniot jump conditions:

$$\text{mass: } \rho_0 u_s = \rho(u_s - u_p) \quad (10)$$

$$\text{momentum: } P_{xx} = P_0 + \rho_0 u_s u_p \quad (11)$$

$$\text{energy: } E_H = E_0 + \frac{1}{2}(P_{xx} + P_0)(V_0 - V) \quad (12)$$

Here, the subscript 0 refers to those quantities in the unshocked initial state. P_{xx} is the normal component of the stress tensor in the shock direction (chosen to be the x direction), $\rho = 1/V$ is the mass per unit volume, u_s is the shock velocity, and u_p is the particle velocity. Equation 10, 11 and 12, lead to the following relations:

$$\frac{u_p}{u_s} = 1 - \frac{V}{V_0} = \epsilon \quad (13)$$

$$u_s = \sqrt{\frac{P_{xx} - P_0}{V_0 - V}} V_0 \quad (14)$$

$$u_p = \sqrt{(P_{xx} - P_0)(V_0 - V)} \quad (15)$$

In the constant-stress Hugoniot method (NP_{xx}Hug),⁶⁹ two extra degrees of freedom are employed to control the system. One is the dimensionless heat-flow variable, ξ , that relaxes the instantaneous internal energy E of the system to the Hugoniot energy given in eq 12. The other is the dimensionless strain-rate stress tensor that equilibrates the component of the stress tensor in the shock propagation direction to the desired value (P_{xx}). The implementation of NP_{xx}Hug can be found elsewhere.⁶⁹ From NP_{xx}Hug simulations, we can derive the Hugoniot state, Hugoniot

elastic limits (HELs), overdriven (OD) points and the $u_p - u_s$ relationship for TKX-50.

The following structures were used in the NP_{xx}Hug simulations to examine the shock response along the [100], [010], and [001] directions.

- For [100] shock simulations, we used the $100 \times 8 \times 14$ supercell containing 537 600 atoms with $a = 533.637 \text{ \AA}$, $b = 96.885 \text{ \AA}$, $c = 90.097 \text{ \AA}$.
- For the [010] shock simulations, we used the $18 \times 50 \times 14$ supercell containing 648 000 atoms was used with $a = 96.885 \text{ \AA}$, $b = 533.637 \text{ \AA}$, $c = 90.097 \text{ \AA}$.
- For the [001] shock simulation, we used the $18 \times 8 \times 80$ supercell containing 552 960 atoms was used with $a = 99.175 \text{ \AA}$, $b = 92.757 \text{ \AA}$, $c = 520.796 \text{ \AA}$.

To test the size effects, we simulated a $100 \times 16 \times 28$ supercell with a doubled cross section under [100] shock compression. We found no size effects as shown in Figure S1 of the Supporting Information.

4.2. Shock Simulation Results. We performed the Hugoniot shock compression simulations along the low index directions [100], [010], and [001] for a range of particle velocities up to $\sim 2.5 \text{ km/s}$ ($\sim 40 \text{ GPa}$). We did not go to higher u_p where chemical reactions might play important roles. Figure 9 shows the shock velocity (u_s) vs normal pressure (P_{xx}) of the

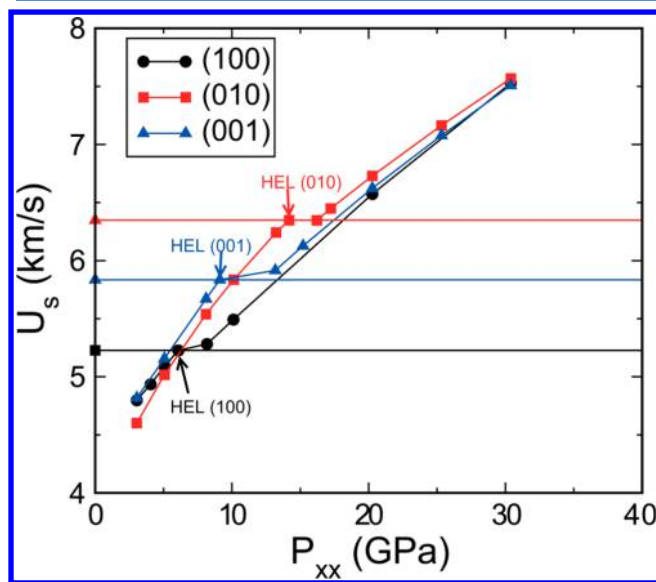


Figure 9. NP_{xx}Hug shock velocity u_s vs P_{xx} in TKX-50 along (100), (010) and (001) planes. Here, the shock velocities of different directions are distinguished by colors: (100) is black, (010) is red, and (001) is blue. Hugoniot elastic limits (HELs) of various shock directions are labeled for viewing convenience. The horizontal dashed lines are drawn to help identification of the overdriven (OD) points, where the plastic wave speed equals u_s^{HEL} .

principal Hugoniot of single crystal TKX-50 for shock propagation along each of the three directions. As expected, for defect-free single crystals, all shock directions exhibit high Hugoniot elastic limits (HELs), with elastic-plastic transition strains in the 13.6–23.3% range corresponding to shock pressures in the 6.1–14.2 GPa range. The HELs are 6.1, 14.2, and 9.1 GPa for [100], [010], and [001] shocks, respectively. The elastic–plastic transition strains and HELs are listed in Table 4. This indicates that single crystal TKX-50 shows anisotropic impact sensitivity: with [010] the most sensitive

Table 4. Calculated Hugoniot Elastic Limit (HEL) and Elastic–Plastic Transition Strains for the TKX-50 Shocked along the [100], [010], and [001] Directions

shock plane	strain ϵ_{HEL}	stress $P_{xx\text{HEL}}$ (GPa)
(100)	0.136	6.1
(010)	0.233	14.2
(001)	0.167	9.1

direction with the highest HEL while [100] is the least sensitive direction with the lowest HEL and [001] is the moderate sensitive direction. Normally, the HELs from MD simulations are higher than the experimental values because we simulate defect free crystals with quite small system size is ($\sim \text{nm}$ scale). In comparison, our HEL predictions on TKX-50 are in the same range as the value of 8 GPa for RDX [100] from other MD simulations.⁷⁰

Figure 10 shows shock velocity (u_s) vs particle velocity (u_p) of the principal Hugoniot. All three orientations exhibit two-

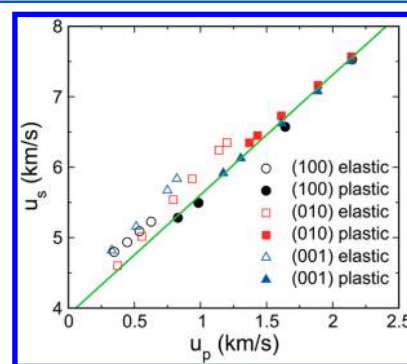


Figure 10. NP_{xx}Hug shock velocities u_s as a function of particle velocity u_p . Data points for different directions are distinguished by various symbols as shown in the figure. The plastic waves and elastic waves are further distinguished by filled and unfilled points. The green line shows a linear $u_s - u_p$ fit using the plastic data points, leading to $u_s = 1.70 + 3.90u_p$.

wave structures characterized by an elastic precursor, followed by a plastic wave whose velocity increases with u_p until it reaches the elastic wave speed at the overdriven (OD) point in the $u_s - u_p$ Hugoniot relation. The OD shock pressures for [100], [010], and [001] directions are 7.2, 16.2, and 11.8 GPa, respectively.

For shock pressures above P_{HELxx} experiments find an elastic-plastic transition characterized by volume collapse in all three directions with a large increase in temperature due to plasticity and shear band formation produced within the plastic zone. We find that the elastic-plastic transition is anisotropic in strain and shear stress, with the [100] orientation exhibiting the lowest shear stress at the HEL (τ_{HEL}), followed by the [010] and [001] directions. The calculated von Mises shear stresses τ [defined as $2\tau = \sigma_{xx} - (\sigma_{yy} + \sigma_{zz})/2$] are 0.56, 1.84, and 1.92 GPa for the [100], [010], and [001] directions, respectively.

The plastic deformation mechanism for stress relaxation is markedly different for the three directions as shown in Figure 11. To examine the atomic local shear, we use maximum relative displacement (MRD),^{10,71} which is defined as $s_i = \mathbf{x}_{ij} - \mathbf{X}_{ij} : |\mathbf{x}_{ij} - \mathbf{X}_{ij}|_{\text{max}}$. Here the \mathbf{x}_{ij} and \mathbf{X}_{ij} vectors correspond to the difference between the current and reference configurations for atoms i and j (slipped neighbors of atom i), respectively. The

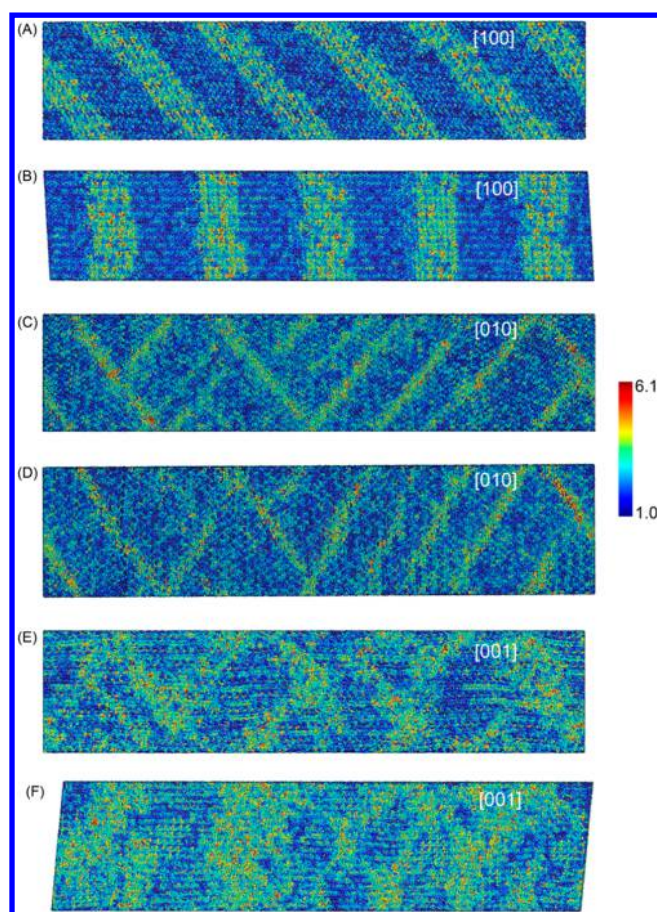


Figure 11. (A–F) Snapshots showing plastic deformation in single crystal TKX-50 shock-loaded along various directions (noted): (A) $P_{xx} = 8.17$ GPa, viewed along (001); (B) $P_{xx} = 8.17$ GPa, viewed along (010); (C) $P_{xx} = 17.22$ GPa, viewed along (001); (D) $P_{xx} = 17.22$ GPa, viewed along (100); (E) $P_{xx} = 13.17$ GPa, viewed along (010); (F) $P_{xx} = 13.17$ GPa, viewed along (100). Color coding refers to the MRD. In (100) shock, (001)/[210] and (010)/[001] slip were observed. In (010) shock, (100)/[021] slip and (001)/[210] slip were observed. In (001) shock, no obvious slip system is observed.

reference configurations are taken to be the preshock structures.

- Figure 11A shows the [100] shock where obvious shear bands are formed with ~ 4.2 nm width. The (001)/[210] and (010)/[001] slip systems were observed in the (100) shock. The MRDs for 3 directions are shown in Figure S2 of the Supporting Information.
- For the [010] shock, Figure 11B shows many more shear bands, but much thinner (~ 1.5 nm) than the [100] shock. Here both (100)/[012] and (001)/[210] slip systems were observed in [010] shock.
- For [001] shock, Figure 11C shows no clear shear band formation.

To illustrate the atomistic mechanisms underlying shear band formation for single crystal TKX-50 under shock compression, we examined the atomic configurations for the [100] and [010] shocks as shown in Figure 12 and Figure 13. For the [100] shock, the maximum shear stress is along the [210] direction, which is $\sim 45^\circ$ to the [100] shock direction. The diolate ($\text{C}_2\text{O}_2\text{N}_8$) $^{2-}$ ring plane is parallel to the [210] direction as shown in Figure 1A, making the slip along (001)/[210] very facile under [100] shock compression. Figure 12 shows clearly

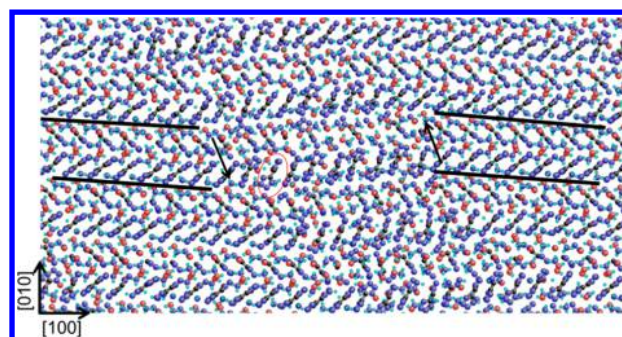


Figure 12. Atomic configuration of TKX-50 for [100] shock compression with $P_{xx} = 8.17$ GPa. The black arrows indicate the slip direction. The black line is to help distinguish the unit cell. The distorted bistetrazole ring is shown in the red circle. The C, H, O, and N atoms are represented by black, cyan, red, and blue balls.

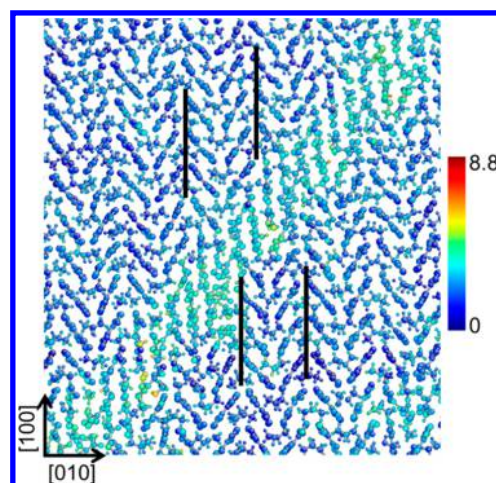


Figure 13. Atomic configuration of TKX-50 for [010] shock compression with $P_{xx} = 17.22$ GPa. The black line is to help distinguish the unit cell along shock direction. Color coding refers to MRD in Å.

the shear band between two crystalline regions being shifted $\sim 1/2$ unit along [210] direction relative to each other. The shear band is ~ 10 unit cells along the [100] direction with width of ~ 5 nm. These results indicate that the shear band under [100] shock compression nucleates from the dislocation with Burgers vector along the [210] direction. We note that the two 5-membered rings rotate ~ 80 degree from each other in the ($\text{C}_2\text{O}_2\text{N}_8$) $^{2-}$ within the shear band region that decreases volume.

For [010] shock compression, the maximum shear stress is also along [210] direction. However, the HEL for [010] shock is much larger than for the [100] shock. This is because the ($\text{C}_2\text{O}_2\text{N}_8$) $^{2-}$ and the neighbor (NH_3OH) $^{1+}$ are compressed directly along the [010] shock direction under shock compression, leading to strong Coulomb interactions between them and thereby making slip difficult.

Figure 13 shows the narrow shear band along [210] direction. The $1/2$ unit shift between the two crystalline regions indicates that the shear band nucleates from the dislocation with Burgers vector of $1/2[210]$ in the (001) plane. We note that the ($\text{C}_2\text{O}_2\text{N}_8$) $^{2-}$ ring is almost aligned to the [100] direction within the shear band.

We did not observe shear band formation for [001] shock compression. This is because the maximum shear stress is not parallel to the $(\text{C}_2\text{O}_2\text{N}_8)^{2-}$ ring plane, as shown in Figure 1(C).

It is well-known that the LJ 12–6 vdW repulsion interactions are too repulsive at short distances. Thus, our FF might overestimate the pressures under shock compression, leading to predicted HELs higher than experiment. However, this would not change our conclusions about anisotropic sensitivity and plastic deformations under shock conditions.

5. SUMMARY

TKX-50 is a newly synthesized explosive that shows promising potential to replace current widely used explosives. To characterize its properties, we developed a flexible classical force field for TKX-50 that reproduces the cell parameters, densities, lattice energy and mechanical properties derived from QM and experiments.

Molecular dynamics simulations were carried out to predict the thermodynamic and mechanical properties, which includes coefficient of thermal expansion (α_p), isothermal compressibility (κ_T), heat capacities (C_v and C_p), and elastic moduli. These data are useful input for multiscale simulations and could be tested experimentally in the future.

Large scale shock simulations were carried out to investigate the elastic limit and plasticity under various shock directions of [100], [010], and [001]. On the basis of the predicted HELs on various directions we expect anisotropic sensitivity: [010] is the sensitive shock direction with the highest HEL, [100] is the insensitive shock direction with the lowest HEL, and [001] is the moderate sensitive shock direction. Structure analysis shows the detailed slip systems leading to plastic deformation in atomic scale.

■ ASSOCIATED CONTENT

Supporting Information

Snapshots showing the plastic deformation in single crystal TKX-50 shock loaded along [100] direction, MRDs of three directions for the [100] shock, and tables of force field parameters, bond stretch parameters, angle parameters, torsion angle parameters, and improper torsion. This material is available free of charge via the Internet at <http://pubs.acs.org>.

■ AUTHOR INFORMATION

Corresponding Author

*(W.A.G.) E-mail: wag@wag.caltech.edu.

Author Contributions

[‡]Those authors contributed equally to this paper

Notes

The authors declare no competing financial interest.

■ ACKNOWLEDGMENTS

We thank Al Stern and Cliff Bedford for suggesting the importance of characterizing TKX-50. This research was funded by ONR (N00014-09-1-0634, Cliff Bedford).

■ REFERENCES

- (1) Fisher, N.; Fisher, D.; Klapötke, T. M.; Piercey, D. G.; Stierstorfer, J. Pushing the Limits of Energetic Materials—the Synthesis and Characterization of Dihydroxylammonium 5,5'-bistetrazole-1,1'-diolate. *J. Mater. Chem.* **2012**, *22*, 20418–20422.
- (2) Golubev, V. K.; Klapoetke, T. M. Comparative Analysis of TKX-50, MAD-X1, RDX and HMX Blasting Performance in One-, Two-

and Three-dimensional Geometry. *New Trends Res. Energ. Mater., Proc. Semin.*, 17th **2014**, *1*, 220–227.

- (3) Golubev, V. K.; Klapoetke, T. M. Comparative Analysis of Shock Wave Action of TKX-50 and Some other Explosives on Various Barriers. *New Trends Res. Energ. Mater., Proc. Semin.*, 17th **2014**, *2*, 672–676.

- (4) Cady, H. H.; Larson, A. C. The Crystal Structure of 1, 3, 5-triamino-2, 4, 6-trinitrobenzene. *Acta Crystallogr.* **1965**, *18*, 485–496.

- (5) Cady, H. H.; Larson, A. C.; Cromer, D. T. The Crystal Structure of α -HMX and a Refinement of the Structure of β -HMX. *Acta Crystallogr.* **1963**, *16*, 617–623.

- (6) Simpson, R. L.; Urtiew, P. A.; Ornellas, D. L.; Moody, G. L.; Scribner, K. J.; Hoffman, D. M. Cl-20 Performance Exceeds That of HMX and Its Sensitivity Is Moderate. *Propellants, Explos., Pyrotech.* **1997**, *22*, 249–255.

- (7) An, Q.; Liu, W. G.; Goddard, W. A., III; Cheng, T.; Zybin, S. V.; Xiao, H. The Initial Steps of Thermal Decomposition of TKX-50 (Dihydroxylammonium 5,5'-bistetrazole-1,1'-diolate) Crystals from Quantum Mechanics. *J. Phys. Chem. C* **2014**, *118*, 27175–27181.

- (8) Bowden, F. P.; Yoffe, A. D. *Initiation and Growth of Explosions in Liquids and Solids*; Cambridge University Press: Cambridge, U.K., 1952.

- (9) Chéret, R. *Detonation of Condensed Explosives*; Springer-Verlag: New York, 1993.

- (10) An, Q.; Zybin, S. V.; Goddard, W. A., III; Jaramillo-Botero, A.; Blanco, M.; Luo, S. N. Elucidation of the Dynamics for Hot-spot Initiation at Nonuniform Interfaces of Highly Shocked Materials. *Phys. Rev. B* **2011**, *84*, 220101(R).

- (11) Holian, B. L.; Germann, T. C.; Maillet, J. B.; White, C. T. Atomistic Mechanism for Hot Spot Initiation. *Phys. Rev. Lett.* **2002**, *89*, 285501.

- (12) An, Q.; Goddard, W. A., III; Zybin, S. V.; Jaramillo-Botero, A.; Zhou, T. T. Highly Shocked Polymer Bonded Explosives at a Nonplanar Interface: Hot-Spot Formation Leading to Detonation. *J. Phys. Chem. C* **2013**, *117*, 26551–26561.

- (13) Field, J. E. Hot Spot Ignition Mechanisms for Explosives. *Acc. Chem. Res.* **1992**, *25*, 489–496.

- (14) Gee, R. H.; Roszak, S.; Balasubramanian, K.; Fried, L. E. Ab Initio Based Force Field and Molecular Dynamics Simulations of Crystalline TATB. *J. Chem. Phys.* **2004**, *120*, 7059–7066.

- (15) Rai, N.; Bhatt, D.; Siepmann, J. I.; Fried, L. E. Monte Carlo Simulations of 1,3,5-Triamino-2,4,6-Trinitrobenzene (TATB): Pressure and Temperature Effects for the Solid Phase and Vapor-liquid Phase Equilibria. *J. Chem. Phys.* **2008**, *129*, 194510.

- (16) Sorescu, D. C.; Rice, B. M.; Thompson, D. L. Intermolecular Potential for the Hexahydro-1,3,5-trinitro-1,3,5-s-triazine Crystal (RDX): A Crystal Packing, Monte Carlo, and Molecular Dynamics Study. *J. Phys. Chem. B* **1997**, *101*, 798–808.

- (17) Agrawal, P. M.; Rice, B. M.; Zheng, L. Q.; Thompson, D. L. Molecular Dynamics Simulations of Hexahydro-1,3,5-trinitro-1,3,5-s-triazine (RDX) Using a Combined Sorescu–Rice–Thompson AMBER Force Field. *J. Phys. Chem. B* **2006**, *110*, 26185–26188.

- (18) Smith, G. D.; Bharadwaj, R. K. Quantum Chemistry Based Force Field for Simulations of HMX. *J. Phys. Chem. B* **1999**, *103*, 3570–3575.

- (19) Borodin, O.; G. D. Smith, G. D.; Sewell, T. D.; Bedrov, D. Polarizable and Nonpolarizable Force Fields for Alkyl Nitrates. *J. Phys. Chem. B* **2008**, *112*, 734–742.

- (20) Neyertz, S.; Mathieu, D.; Khanniche, S.; Brown, D. An Empirically Optimized Classical Force-Field for Molecular Simulations of 2,4,6-Trinitrotoluene (TNT) and 2,4-Dinitrotoluene (DNT). *J. Phys. Chem. A* **2012**, *116*, 8374–8381.

- (21) Cawkwell, M. J.; Romos, K. J.; Hooks, D. E.; Sewell, T. D. Homogeneous Dislocation Nucleation in Cyclotrimethylene Trinitramine under Shock Loading. *J. Appl. Phys.* **2010**, *107*, 063512.

- (22) Ramos, K. J.; Hooks, D. E.; Sewell, T. D.; Cawkwell, M. J. Anomalous Hardening under Shock Compression in (021)-oriented Cyclotrimethylene Trinitramine Single Crystals. *J. Appl. Phys.* **2010**, *108*, 066105.

- (23) Munday, L. B.; Chung, P. W.; Rice, B. M.; Solares, S. D. Simulations of High-Pressure Phases in RDX. *J. Phys. Chem. B* **2011**, *115*, 4378–4386.
- (24) Sewell, T. D.; Menikoff, R.; Bedrov, D.; Smith, G. D. A Molecular Dynamics Simulation Study of Elastic Properties of HMX. *J. Chem. Phys.* **2003**, *119*, 7417–7426.
- (25) Hooper, J. B.; Borodin, O. Molecular Dynamics Simulations of *N,N,N,N*-tetramethylammonium Dicyanamide Plastic Crystal and Liquid using a Polarizable Force Field. *Phys. Chem. Chem. Phys.* **2010**, *12*, 4635–4643.
- (26) Strachan, A.; van Duin, A. C. T.; Chakraborty, D.; Dasgupta, S.; Goddard, W. A., III. Shock Waves in High-energy Materials: The Initial Chemical Events in Nitramine RDX. *Phys. Rev. Lett.* **2003**, *91*, 098301.
- (27) An, Q.; Goddard, W. A., III; Zybin, S. V.; Luo, S. N. Inhibition of Hotspot Formation in Polymer Bonded Explosives Using an Interface Matching Low Density Polymer Coating at the Polymer–Explosive Interface. *J. Phys. Chem. C* **2014**, *118*, 19918–19928.
- (28) Zybin, S. V.; Goddard, W. A., III; Xu, P.; van Duin, A. C. T.; Thompson, A. P. Physical Mechanism of Anisotropic Sensitivity in Pentaerythritol Tetranitrate from Compressive-shear Reaction Dynamics Simulations. *Appl. Phys. Lett.* **2010**, *96*, 081918.
- (29) An, Q.; Liu, Y.; Zybin, S. V.; Kim, H.; Goddard, W. A., III. Anisotropic Shock Sensitivity of Cyclotrimethylene Trinitramine (RDX) from Compress-and-shear Reactive Dynamics. *J. Phys. Chem. C* **2012**, *116*, 10198–10206.
- (30) Zhang, L. Z.; van Duin, A. C. T.; Zybin, S. V.; Goddard, W. A., III. Thermal Decomposition of Hydrazines from Reactive Dynamics Using the ReaxFF Reactive Force Field. *J. Phys. Chem. B* **2009**, *113*, 10770–10778.
- (31) Becke, A. D. Density-functional Exchange-energy Approximation with Correct Asymptotic Behavior. *Phys. Rev. A* **1988**, *38*, 3098–3100.
- (32) Becke, A. D. Density-functional Thermochemistry. III. The Role of Exact Exchange. *J. Chem. Phys.* **1993**, *98*, 5648–5652.
- (33) Bochevarov, A. D.; Harder, E.; Hughes, T. F.; Greenwood, J. R.; Braden, D. A.; Philipp, D. M.; Rinaldo, D.; Halls, M. D.; Zhang, J.; Friesner, R. A. Jaguar: A high-performance quantum chemistry software program with strengths in life and materials sciences. *Int. J. Quantum Chem.* **2013**, *113*, 2110–2142.
- (34) Kim, H.; Choi, J. M.; Goddard, W. A., III. Universal Correction of Density Functional Theory to Include London Dispersion (up to L_r , Element 103). *J. Phys. Chem. Lett.* **2012**, *3*, 360–363.
- (35) Kresse, G.; Hafner, J. Ab Initio Molecular Dynamics for Liquid Metals. *Phys. Rev. B* **1993**, *47*, 558–561.
- (36) Kresse, G.; Furthmüller, J. Efficiency of Ab-Initio Total Energy Calculations for Metals and Semiconductors Using a Plane-Wave Basis Set. *Comput. Mater. Sci.* **1996**, *6*, 15–50.
- (37) Kresse, G.; Furthmüller, J. Efficient Iterative Schemes for Ab Initio Total-Energy Calculations Using a Plane-Wave Basis Set. *Phys. Rev. B* **1996**, *16*, 11169–11186.
- (38) Kresse, G.; Joubert, D. From Ultrasoft Pseudopotentials to the Projector Augmented-Wave Method. *Phys. Rev. B* **1999**, *59*, 1758–1775.
- (39) Elstner, M.; Porezag, D.; Jungnickel, G.; Elsner, J.; Haugk, M.; Frauenheim, Th.; Suhai, S.; Seifert, G. Self-Consistent-Charge Density-Functional Tight-Binding Method for Simulations of Complex Materials Properties. *Phys. Rev. B* **1998**, *58*, 7260–7268.
- (40) Gaus, M.; Goez, A.; Elstner, M. Parametrization and Benchmark of DFTB3 for Organic Molecules. *J. Chem. Theory. Comput.* **2013**, *9*, 338–354.
- (41) Cornell, W. D.; Cieplak, P.; Bayly, C. L.; Gould, I. R.; Merz, K. M.; Ferguson, D. M.; Spellmeyer, D. C.; Fox, T.; Caldwell, J. W.; Kollman, P. A. A Second Generation Force Field for the Simulation of Proteins and Nucleic Acids. *J. Am. Chem. Soc.* **1995**, *117*, 5179–5197.
- (42) http://www.aeontechnology.com/Product_DFF.php.
- (43) Dasgupta, S.; Goddard, W. A., III. Hessian-Biased Force Fields from Combining Theory and Experiment. *J. Chem. Phys.* **1989**, *90*, 7207–7215.
- (44) Dasgupta, S.; Yamasaki, T.; Goddard, W. A., III. The Hessian Biased Singular Value Decomposition Method for Optimization and Analysis of Force Fields. *J. Chem. Phys.* **1996**, *104*, 2898–2920.
- (45) Dupradeau, F. Y.; Pigache, A.; Zaffran, T.; Savineau, C.; Lelong, R.; Grivel, N.; Lelong, D.; Rosanski, W.; Cieplak, P. The R.E.D. Tools: Advances in RESP and ESP Charge Derivation and Force Field Library Building. *Phys. Chem. Chem. Phys.* **2010**, *12*, 7821–7839.
- (46) Mulliken, R. S. Electronic Population Analysis on LCAO–MO Molecular Wave Functions. I. *J. Chem. Phys.* **1955**, *23*, 1833–1840.
- (47) Löwdin, P. O. On the Non-Orthogonality Problem Connected with the Use of Atomic Wave Functions in the Theory of Molecules and Crystals. *J. Chem. Phys.* **1950**, *18*, 365–375.
- (48) Bader, R. F. W.; Nguyen-Dang, T. T.; Per-Olov, L. *Adv. Quantum Chem.* **1981**, *14*, 63.
- (49) Hagler, A. T.; Huler, E.; Lifson, S. Energy Functions for Peptides and Proteins. I. Derivation of a Consistent Force Field including the Hydrogen Bond from Amide Crystals. *J. Am. Chem. Soc.* **1974**, *96*, 5319–5327.
- (50) Jorgensen, W. J.; Tirado-Rives, J. The OPLS [Optimized Potentials for Liquid Simulations] Potential Functions for Proteins, Energy Minimizations for Crystals of Cyclic Peptides and Crambin. *J. Am. Chem. Soc.* **1988**, *110*, 1657–1666.
- (51) Besler, B. H.; Merz, K. M.; Kollman, P. A. Atomic Charges Derived from Semiempirical Methods. *J. Comput. Chem.* **1990**, *11*, 431–439.
- (52) Momany, F. A. Determination of Partial Atomic Charges from Ab Initio Molecular Electrostatic Potentials. Application to Formamide, Methanol, and Formic Acid. *J. Phys. Chem.* **1978**, *82*, 592–601.
- (53) Cox, S. R.; Williams, D. E. Representation of the Molecular Electrostatic Potential by a Net Atomic Charge Model. *J. Comput. Chem.* **1981**, *2*, 304–323.
- (54) Singh, U. C.; Kollman, P. A. An Approach to Computing Electrostatic Charges for Molecules. *J. Comput. Chem.* **1984**, *5*, 129–145.
- (55) Chirlian, L. E.; Francel, M. M. Atomic Charges Derived from Electrostatic Potentials: A Detailed Study. *J. Comput. Chem.* **1987**, *8*, 894–905.
- (56) Williams, D. E. In *Reviews in Computational Chemistry*; John Wiley & Sons, Inc.: Hoboken, NJ, 2007; p 219.
- (57) Jakalian, A.; Bush, B. L.; Jack, D. B.; Bayly, C. I. Fast, Efficient Generation of High-quality Atomic Charges. AM1-BCC model: I. Method. *J. Comput. Chem.* **2000**, *21*, 132–146.
- (58) Jakalian, A.; Jack, D. B.; Bayly, C. I. Fast, Efficient Generation of High-quality Atomic Charges. AM1-BCC Model: II. Parameterization and Validation. *J. Comput. Chem.* **2002**, *23*, 1623–1641.
- (59) Plimpton, S. Fast Parallel Algorithms for Short-Range Molecular Dynamics. *J. of Comput. Phys.* **1995**, *117*, 1–19.
- (60) Hockney, R. W.; Eastwood, J. W. *Computer Simulation Using Particles*; 2nd ed.; IOP: Bristol, U.K., 1988.
- (61) Shinoda, W.; Shiga, M.; Mikami, M. Rapid Estimation of Elastic Constants by Molecular Dynamics Simulation under Constant Stress. *Phys. Rev. B* **2004**, *69*, 134103.
- (62) Pascal, T. A.; Lin, S. T.; Goddard, W. A., III. Thermodynamics of Liquids: Standard Molar Entropies and Heat Capacities of Common Solvents from 2PT Molecular Dynamics. *Phys. Chem. Chem. Phys.* **2011**, *13*, 169–181.
- (63) Lin, S. T.; Maiti, P. K.; Goddard, W. A., III. Two-Phase Thermodynamic Model for Efficient and Accurate Absolute Entropy of Water from Molecular Dynamics Simulations. *J. Phys. Chem. B* **2010**, *114*, 8191–8198.
- (64) Allen, P.; Tildesley, D. J. *Computer Simulation of Liquids*; Clarendon Press: London, 1989.
- (65) Sun, J.; Shu, X. Y.; Liu, Y.; Zhang, H. B.; Liu, X. F.; Jiang, Y.; Kang, B.; Xue, C.; Song, G. B. Investigation on the Thermal Expansion and Theoretical Density of 1,3,5-Trinitro-1,3,5-Triazacyclohexane. *Propellants, Explos., Pyrotech.* **2011**, *36*, 341–346.

- (66) Rylance, J.; Stubley, D. Heat Capacities and Phase Transitions of Octahydro- 1,3,5,7-tetranitro-1,3,5,7-tetrazocine (HMX). *Thermochim. Acta* **1975**, *13*, 253–259.
- (67) Miller, M. S. *Thermophysical Properties of Six Solid Gun Propellants*; Report No. ARL-TR-1322; ARL: Adelphi, MD, 1997.
- (68) Nye, J. F. *Physical Properties of Crystals: Their Representation by Tensors and Matrices*; Clarendon Press: Oxford, U. K., 1985.
- (69) Ravelo, R.; Holian, B. L.; Germann, T. C.; Lomdahl, P. S. Constant-stress Hugoniot Method for Following the Dynamical Evolution of Shocked Matter. *Phys. Rev. B* **2004**, *70*, 014103.
- (70) Bedrov, D.; Hooper, J. B.; Smith, G. D.; Sewell, T. D. Shock-induced Transformations in Crystalline RDX: A Uniaxial Constant-Stress Hugoniot Molecular Dynamics Simulation Study. *J. Chem. Phys.* **2009**, *131*, 034712.
- (71) Zimmerman, J.; Kelchner, A. C. L.; Klein, P. A.; Hamilton, J. C.; Foiles, S. M. Surface Step Effects on Nanoindentation. *Phys. Rev. Lett.* **2001**, *87*, 165507.
- (72) Glasser, L.; Jenkins, H. D. B.; Klapötke, T. M. Is the Volume-Based Thermodynamics (VBT) Approach Valid for the Estimation of the Lattice Enthalpy of Salts Containing the S, S'-(Tetrazolate-1N-oxide) Dianion? *Z. Anorg. Allg. Chem.* **2014**, *640*, 1297–1299.